Materials Today Nano 31 (2025) 100655

Contents lists available at ScienceDirect

Materials Today Nano

journal homepage: www.sciencedirect.com/journal/materials-today-nano

Controlling stability and size of amorphous magnesium calcium phosphate particles

Debora Briganti [a], Melissa Saibene [b], Giancarlo Capitani [c], Rita Gelli [a,*], Francesca Ridi [a]

[a] Department of Chemistry "Ugo Schiff" and CSGI, University of Florence, via della Lastruccia 3, Sesto Fiorentino, Florence, 50019, Italy
[b] PMiB, Microscopy Platform, University of Milano-Bicocca, Piazza della Scienza 2, Milan, 20126, Italy
[c] Department of Earth and Environmental Sciences, University of Milano-Bicocca, Piazza della Scienza 4, Milan, 20126, Italy

ARTICLE INFO

Keywords:
Amorphous magnesium-calcium phosphate
Nanoparticles
Polyacrylic acid
Stability
Dispersibility
Crystallization
Size control

ABSTRACT

The development of nanoparticles with tunable size and stability is crucial for the development of safe and effective drug delivery systems. Amorphous Magnesium Calcium Phosphate (AMCP) nanoparticles offer a promising solution due to their biocompatibility, biodegradability, and ability to load bioactive substances. However, their successful application is hindered by two main limitations: the tendency of the metastable amorphous phase to crystallize into more thermodynamically stable forms and the propensity for aggregation in the absence of stabilizing agents, which compromises their nanoscale properties. This study focuses on the preparation and characterization of AMCP nanoparticles stabilized with polyacrylic acid (PAA), with the purpose of understanding whether variations in the synthetic Ca/Mg ratio and PAA molecular weight (M_w) influence nanoparticles' physico-chemical properties such as size, crystallinity, dispersibility and stability, along with their solubility in different pH environments, to explore potential applications in the pharmacological field.

The results reveal that PAA acts as a remarkable stabilizing agent for AMCPs, significantly reducing aggregation and enhancing dispersibility. Stability and size were strongly influenced by Ca/Mg ratio and PAA M_w, demonstrating the crucial interplay between these factors in nanoparticles design. Incorporating PAA not only delayed the thermal crystallization process but also improved the resistance of AMCPs to dissolution in acidic environments, highlighting their potential for pH-responsive drug delivery applications. Additionally, a higher magnesium content was found to enhance the stability of the amorphous phase, while PAA effectively prevented the transformation of AMCP into hydroxyapatite under physiological conditions, further reinforcing its role in achieving the desired nanoparticle properties.

1. Introduction

Calcium Phosphates (CP) represent a class of inorganic materials of great interest due to their unique physico-chemical, biological, and structural properties. They are the primary inorganic components of vertebrate hard tissues, such as bones and teeth, whose mineral phase closely resembles synthetic hydroxyapatite (HA) [1–3]. A notable feature of biological apatites is their ability to incorporate foreign ions, which can be either included into the crystal lattice or simply adsorbed onto the crystal surface [3]. In addition to HA, various other CP phases are found in biological tissues, including amorphous calcium phosphate (ACP), amorphous magnesium calcium phosphate (AMCP), dicalcium phosphate dihydrate (DCPD), tricalcium phosphate (TCP), and octacalcium phosphate (OCP) [2–4]. Due to their similarity to the inorganic phases of biomineralized tissues, CPs and their ion-substituted derivatives exhibit high biocompatibility and bioactivity, making them

Abbreviations: ACC, Amorphous Calcium Carbonate; ACP, Amorphous Calcium Phosphate; AMCP, Amorphous Magnesium-Calcium Phosphate; AMCP_PAA, Amorphous Magnesium-Calcium Phosphate stabilized with PAA; BF-TEM, Bright Field-Transmission Electron Microscopy; CP, Calcium Phosphates; CP_PAA, Calcium Phosphates particles stabilized with PAA; DCPD, Dicalcium Phosphate Dihydrate; DLS, Dynamic Light Scattering; EDS, Energy-Dispersive X-ray Spectroscopy; FE-SEM, Field Emission-Scanning Electron Microscopy; FT-IR, Fourier Transform-Infrared Spectroscopy; HA, Hydroxyapatite; LC, Loading Capacity; LE, Loading Efficiency; M_w, Molecular Weight; OCP, Octacalcium Phosphate; PAA, polyacrylic acid; $PAA_{1.2kDa}$, polyacrylic acid with average molecular weight of 1200 Da; PAA_{8kDa}, polyacrylic acid with average molecular weight of 8000 Da; PAA_{15kDa}, polyacrylic acid with average molecular weight of 15000 Da; SAED, Selected Area Electron Diffraction; TCP, tricalcium phosphate; TGA, Thermogravimetry Analysis; XRD, X-Ray Diffraction.

* Corresponding author.
E-mail address: rita.gelli@unifi.it (R. Gelli).

https://doi.org/10.1016/j.mtnano.2025.100655
Received 28 April 2025; Received in revised form 27 June 2025; Accepted 9 July 2025
Available online 10 July 2025

materials of great interest for applications in multiple areas. CPs have demonstrated their potential as drug delivery systems: relevant examples include the work from Fu et al., who developed biodegradable and pH-responsive Mn-doped CP nanoparticles containing glucose oxidase and doxorubicin for orchestrated cooperative cancer treatment [5]. Interestingly, the intracellular dissolution of CP nanoparticles occurring upon uptake in the acidic environment of endosomes/lysosomes can induce intracellular Ca^{2+} overload and apoptosis, to be exploited in cancer therapy [6,7]. CPs were also recently used to co-deliver immunotherapy agents to treat melanoma [8] and, beyond cancer therapy, rapamycin-loaded CP nanoparticles demonstrated their efficacy in the treatment of atherosclerosis [9]. Out of note, CP nanoparticles have been used for decades to prepare complexes with nucleic acids for gene therapy, as it was recently reviewed by Xing et al. [10], and are also promising as vehicles for the delivery of vaccines [11].

Among different type of CPs, the amorphous forms, ACP and AMCP, have attracted increasing interest due to their biological relevance, as their presence has been documented in dental enamel and in the mammalian intestine, where they play a key role in immune surveillance [12]. These amorphous phases are characterized by a disordered structure lacking long-range order and often play central roles in processes such as biomineralization [13–16]. In many studies, they have shown greater bioactivity compared to their crystalline counterparts [4]. However, they are metastable phases, characterized by high solubility and low stability, leading to their eventual transition into more thermodynamically stable crystalline forms [2,17]. Therefore, stabilizing ACP and AMCP represents a crucial challenge in the design of functional materials for pharmaceutical applications.

Another critical aspect is particles' size, a key parameter for modulating their functional properties and *in vivo* pathways. In the biomedical field, the control of particle size, ideally around 100 nm, is essential to ensure stability, loading capacity, and efficient biodistribution [18–20]. Regarding the size of ACP particles, their constitutive structural unit is the so-called Posner's cluster, $Ca_9(PO_4)_6$, which has a diameter of approximately 1 nm [21]. During co-precipitation, numerous Posner's clusters rapidly aggregate to form spherical ACP particles with diameters typically ranging from 30 to 100 nm. These primary nanoparticles further assemble rapidly into chain-like aggregates that can reach micrometer-scale dimensions [22]. Moreover, in contact with the mother liquor and depending on experimental conditions, ACP is metastable and readily transforms into more stable crystalline phases, which can display different solubilities, colloidal stabilities and surface chemistry [23–25]. Therefore, strategies to improve their stability both in terms of size and amorphous nature are crucial to preserve the structural features of ACP and AMCP nanoparticles. The use of stabilizing agents is an effective solution to prevent crystallization. Additionally, polymers containing functional groups able to interact with calcium ions can modulate nanoparticles' size by inhibiting or delaying the aggregation process. Several approaches have been reported in the literature for stabilizing calcium phosphate nanoparticles using organic additives such as cyclodextrins, ethylene glycol, proteins, polymers, and bisphosphonates [17,26–31]. It is also known that magnesium influences particles' stability and size: magnesium stabilizes amorphous phases by delaying crystallization, while an optimal Ca/Mg ratio modulates nucleation and growth, affecting the final particle size [32,33]. Besides magnesium, other ions affect the stability of ACP: for instance, it was observed that in the presence of fluoride the aggregation of ACP nanospheres and the nucleation of crystalline phases are retarded, thus stabilizing the amorphous phase [34]. Notably, naturally occurring small organic molecules such as citrate can stabilize ACP [35–37]. This stabilization plays a key role in bone mineralization, as citrate constitutes 2–5 % of the organic content in bone and is tightly bound to apatite nanocrystals. The combined effect of fluoride and citrate is relevant in the context of enamel biomineralization processes and to produce biomimetic bioceramics [38–40].

Polycarboxylate polymers such as polyacrylic acid (PAA) can also be used to enhance amorphous phase stability and to control particle size. PAA has been extensively studied for biomedical applications thanks to its biocompatibility, biodegradability and pH responsiveness [41,42]. Additionally, PAA is used in wound healing and biomedical coatings, providing protective and adhesive properties [43,44]. PAA has been investigated for its role on the formation and stability of amorphous calcium carbonate (ACC), and demonstrated its ability to generate ACC-functionalized nanoparticles [45–49]. On a related note, similar carboxylated polymers such as polyaspartic acid have demonstrated their ability to stabilize ACC and regulate its crystallization pathways, showcasing the significance of the process in the context of biomineralization [50–53]. Compared to ACC, the use of PAA to stabilize ACP has been investigated to a much lesser extent [26,54]. Moreover, most studies in the literature concerning PAA role towards ACC and ACP focus on PAA's stabilizing effect towards the amorphous phase, while little attention was devoted so far to the exploration of its role in particles' size control [26,46]. Although PAA interacts with particles' surface through calcium ion chelation, preventing aggregation and improving colloidal suspension stability, it is crucial that stabilized particles maintain their size and functional properties even after processes such as drying and redispersion in aqueous media. Currently, most studies dealing with CP nanoparticles only describe their size during synthesis, neglecting the fate of the particles when dried and dispersed again in solution, or providing unclear redispersion methods [17,26,27,30,55]. This aspect is though fundamental for the application of such systems in, for instance, the biomedical field, where nanoparticles loaded with active molecules or targeting agents are often prepared, dried and dispersed in relevant media for *in vitro* tests with cells or even for *in vivo* administration. An interesting example in this respect was reported in the work by Adamiano et al., in which HA nanoparticles were dispersed in a 5 % glucose solution before *in vivo* administration to mice [56].

Limited information is available in the literature regarding CP particles' size after redispersion and possible strategies to improve this process. Moreover, the combined effects of varying PAA molecular weight and Ca/Mg ratio on the size, dispersibility, and stability of calcium and magnesium phosphate particles have not yet been investigated.

This study reports the synthesis and characterization of PAA-stabilized amorphous magnesium calcium phosphate nanoparticles (AMCP_PAA). The aim is to evaluate the influence of variations in the Ca/Mg ratio and the molecular weight (M_w) of PAA on particles' properties. To this end, a systematic analysis was conducted through the synthesis of 12 different formulations, varying the concentrations of precursor solutions to achieve four Ca/Mg ratios (0.2, 0.4, 0.6, and 0.8), each combined with three different types of PAA (M_w of 1.2, 8, and 15 kDa). The resulting particles were analyzed in terms of size, dispersibility, amorphous or crystalline nature, morphology, elemental composition, thermal behavior, stability, and solubility in environments with different pH values, to gain an in-depth understanding of their physicochemical properties and potential pharmaceutical applications as drug delivery systems.

2. Materials and methods

2.1. Materials

Calcium chloride ($CaCl_2$, ≥98 %), magnesium chloride hexahydrate ($MgCl_2{\cdot}6H_2O$, ≥99 %), sodium chloride (NaCl, ≥99 %), potassium chloride (KCl, ≥99 %), potassium dihydrogen phosphate (KH_2PO_4, ≥99 %), sodium phosphate dibasic dodecahydrate ($Na_2HPO_4{\cdot}12H_2O$, ≥99 %), acetic acid (CH_3COOH, ≥99.7 %), sodium polyacrylate (PAA; $PAA_{1.2kDa}$, M_w = 1200 Da, 45 % wt in H_2O; PAA_{8kDa}, M_w = 8000 Da, 45 % wt in H_2O; PAA_{15kDa}, M_w = 15000 Da, 35 % wt in H_2O), potassium bromide (KBr, FT-IR grade), hydrochloric acid (HCl, 37 %) and acetaminophen (paracetamol - $C_8H_9NO_2$, ≥99 %) were purchased from Sigma-Aldrich (Milan, Italy). Sodium acetate (CH_3COONa, ≥99 %) was

obtained from Fluka (Milan, Italy). Milli-Q grade water (Millipore, resistivity 18.2 MΩ cm at 25 °C) was used during all the experiments.

2.2. Preparation of AMCP_PAA nanoparticles

AMCP_PAA nanoparticles were prepared by precipitation from an aqueous solution, following a method readapted from the literature [26].

Briefly, 100 mL of solution A (A_1 to A_4, see Table 1) was mixed with 100 mL of solution B (B_1 to B_4, see Table 2), at room temperature. The resulting mixture was stirred for 1 h; subsequently, the colloidal dispersion was distributed into six Falcon tubes, and 20 % (v/v) ethanol was added to each tube to promote nanoparticles precipitation. The precipitate was then collected by centrifugation at 9500 rpm for 15 min. At the end the pellet in each Falcon tube was washed with 30 mL of Milli-Q water. The resulting pellet was then freeze-dried for 24 h, at −55 °C and ~100 mTorr (VirTis BenchTop freeze-dryer, NY, USA). The resulting samples are listed in Table 3 with their respective nomenclature.

2.3. Preparation of control particles (CP, CP_PAA, and AMCP)

Control samples (*i.e.* without either PAA or Mg) were synthesized following a procedure similar to the one used for AMCP_PAA nanoparticles described in section 2.2. Specifically, CP and AMCP particles (*i.e.* control samples without PAA) were prepared by mixing 100 mL of solution A (A_0 to A_4, see Table 1) with 100 mL of solution B_0 (see Table 2), while CP_PAA nanoparticles (*i.e.* control samples without Mg) were obtained by combining 100 mL of solution A_0 (see Table 1) with 100 mL of solution B (B_1 to B_3, see Table 2). All samples were then processed using the same protocol as AMCP_PAA.

2.4. Characterization techniques

2.4.1. Dynamic light scattering (DLS)

DLS measurements were performed using a 90 Plus Particle Sizing instrument (Brookhaven Instruments) at 25 °C, with a detection angle of 90°. Each measurement consisted of 10 runs, each lasting 10 s.

The light source was a solid state laser (λ = 653 nm) and the scattered intensity was detected by an avalanche photodiode detector. The reported hydrodynamic diameters in this work represent the arithmetic mean and the corresponding standard deviation of the average diameters obtained from each run analyzed through cumulant analysis.

2.4.2. Laser granulometry

The size distribution of control samples ($S_{0.8}$, $S_{0.6}$, $S_{0.4}$ and $S_{0.2}$) was analyzed by means of laser granulometry, using a Mastersizer 3000 (Malvern) with a Hydro SM dispersion unit. Water was used as a dispersant, while the optical properties of calcium phosphate were: density 3.14 g/mL, absorption coefficient 0.1, refractive index 1.63. Measurements were conducted using a stirring speed of 1800 rpm, and for each sample 15 runs of 10 s each (and 5 s of delay) were averaged. Before adding the sample, the background (water) was measured for 15 s, then samples' dispersion was added until an obscuration of ~3 % was attained. The results are expressed as D_{10}, D_{50} and D_{90} (average ± standard deviation of 15 measurements).

Table 1
Composition of the solutions A used for the syntheses. The values of the Ca/Mg salts molar ratio were approximated to one decimal place.

Solution A	Ca/Mg salts molar ratio	$CaCl_2$ [mM]	$MgCl_2{\cdot}6H_2O$ [mM]
A_0	–	14.0	0
A_1	0.8	6.2	7.8
A_2	0.6	5.2	8.8
A_3	0.4	4.0	10.0
A_4	0.2	2.3	11.7

Table 2
Composition of the solutions B used for the syntheses.

Solution B	M_w PAA (kDa)	Repetitive unit concentration [mM]	$Na_2HPO_4{\cdot}12\ H_2O$ [mM]
B_0	–	–	200
B_1	1.2	9	200
B_2	8	9	200
B_3	15	9	200

Table 3
Summary of the prepared samples and their corresponding nomenclature.

Solution	B_0	B_1	B_2	B_3
A_0	S_{Mg0}	$S_{Mg0\_1.2kDa}$	S_{Mg0_8kDa}	S_{Mg0_15kDa}
A_1	$S_{0.8}$	$S_{0.8\_1.2kDa}$	$S_{0.8\_8kDa}$	$S_{0.8\_15kDa}$
A_2	$S_{0.6}$	$S_{0.6\_1.2kDa}$	$S_{0.6\_8kDa}$	$S_{0.6\_15kDa}$
A_3	$S_{0.4}$	$S_{0.4\_1.2kDa}$	$S_{0.4\_8kDa}$	$S_{0.4\_15kDa}$
A_4	$S_{0.2}$	$S_{0.2\_1.2kDa}$	$S_{0.2\_8kDa}$	$S_{0.2\_15kDa}$

2.4.3. Field Emission-Scanning Electron Microscopy (FE-SEM)

FE-SEM analysis was performed using a Zeiss SIGMA FE-SEM (Carl Zeiss Microscopy GmbH, Jena, Germany). The powders were mounted on aluminum stubs using conductive tape. Micrographs were acquired with an accelerating voltage of 2 kV, a sample-detector distance of ~2 mm, aperture of 10 μm, and an In-Lens detector.

EDS spectroscopy was performed using an X-act Silicon Drift Detector (Oxford Instruments, England). The spectra were collected with an accelerating voltage of 10 kV, a working distance of approximately 8 mm, and an aperture size of 60 μm.

2.4.4. Bright Field Transmission Electron Microscopy (BF-TEM)

BF-TEM analysis was performed with a TEM JEOL JEM 2100 Plus (JEOL, Japan) with a LaB_6 emitter, with an acceleration voltage of 200 kV. The instrument is equipped with an 8-megapixel Gatan (Gatan, USA) Rio Complementary Metal-Oxide-Superconductor (CMOS) camera. Samples were prepared by depositing a droplet (5 μL) of sonicated particles dispersed in ethanol on TEM carbon-coated copper grids and let dry in air. During imaging, the exposure time was limited to prevent any possible beam damage.

2.4.5. Fourier Transform-Infrared spectroscopy (FT-IR)

FT-IR spectra were collected using a Bio-Rad FTS-40 spectrophotometer (Hercules, CA, USA). The samples were analyzed in KBr pellets, prepared by mixing (1.00 ± 0.05) mg of sample with (100 ± 1) mg of KBr. The spectra were acquired in the range 4000–400 cm^{-1} using a resolution of 2 cm^{-1}, 64 scans and scan delay of 600 s.

2.4.6. X-ray diffraction (XRD)

XRD patterns were collected using a D8 Advance with DAVINCI design (Bruker, Milan, Italy), using as X-ray source the Cu Kα radiation (wavelength 1.54 Å), at 40 kV and 40 mA, a 2θ range of 5°–50°, a step size of 0.03°, and a time/step of 0.3 s. Samples were grinded with agate mortar and pestle and flattened onto a Si zero-background sample holder.

2.4.7. Thermal analysis

Thermal analysis was performed using a SDT650 (Simultaneous Differential Scanning Calorimetry and Thermogravimetric Analysis) from TA Instruments (New Castle, DE, USA) to monitor both weight loss and heat flow profiles. Samples were placed in alumina pan and measured under N_2 atmosphere (flow rate: 100 mL/min) from room temperature to 1000 °C (at 10 °C/min) for the powder samples. The PAA solutions, however, were treated differently, following a three-stage procedure: an initial heating ramp from room temperature to 80 °C (at 10 °C/min) followed by equilibration at 80 °C for 30 min to ensure

complete evaporation of the water solution, and a final heating ramp from 80 to 1000 °C at 10 °C/min.

The amount of PAA in the samples was determined by analyzing the residual mass percentages of AMCP (R_{AMCP}), AMCP_PAA (R_{AMCP_PAA}), and PAA (R_{PAA}) according to Equation (1):

$$\frac{R_{AMCP\_PAA}}{100} = x\frac{R_{PAA}}{100} + (1-x)\frac{R_{AMCP}}{100} \quad \text{(Equation 1)}$$

where x represents the fraction of PAA, and (1-x) corresponds to the fraction of AMCP in the composite sample.

2.5. Dispersibility evaluation

The freeze-dried samples were dispersed in Milli-Q water at a concentration of 0.5 mg/mL and sonicated using two different devices: a probe sonicator (Branson 450 Digital Sonifier) and a bath sonicator (Falc Instruments). For probe sonication, the samples were processed for 5 min at 30 % amplitude and power of 400 W. For bath sonication, the samples were treated for 30 min at room temperature, operating at a frequency of 59 kHz and 100 % power.

2.6. Stability assessment

To evaluate the stability of the samples towards crystallization and dissolution in different conditions, AMCP_PAA nanoparticles and AMCP particles (controls) were dispersed in buffer solutions at two different pH values (5.0 and 7.4). Two buffers were prepared for this purpose. The acetate buffer solution (pH 5.0) was obtained by dissolving sodium acetate (CH_3COONa, 70 mM) and acetic acid (CH_3COOH, 30 mM) to reach a final volume of 200 mL. The PBS buffer solution (pH 7.4) was prepared by dissolving sodium chloride (NaCl, 137 mM), potassium chloride (KCl, 2.7 mM), potassium dihydrogen phosphate (KH_2PO_4,10 mM), and sodium phosphate dibasic ($Na_2HPO_4{\cdot}12H_2O$ 1.8 mM) to achieve a final volume of 200 mL. These buffers were chosen to replicate conditions typically encountered in the human body, namely pH 7.4 representing physiological conditions and pH 5.0 mimicking more acidic environments, such as those found in intracellular compartments (e.g., endosomes and lysosomes) and in tumor microenvironments [57,58].

The samples were initially dispersed in the two buffer solutions at a concentration of 0.5 mg/mL, sonicated for 5, 10, and 15 min at 37 °C with a frequency of 59 kHz and 100 % power using a bath sonicator (Falc Instruments). The samples in PBS buffer were then maintained under stirring in a water bath at 37 °C to simulate physiological temperature and to study their long-term stability. Aliquots of 6 mL were collected at various time intervals: 5 min, 10 min, 1 h, 6 h, 24 h, 1 day, 2 days, 3 days, and 5 days. The 6 mL were divided into six Eppendorf tubes, centrifuged for 5 min at 15000 rpm, washed with a total of 6 mL of water, and lyophilized. The samples were then analyzed by FT-IR, following the procedure described in 2.4.5.

2.7. Drug loading, redispersion performance, and release experiments

To evaluate the performance of AMCP_PAA nanoparticles as a drug carrier in a realistic scenario, a representative sample ($S_{0.8\_15kDa}$) was loaded with paracetamol as a model drug. Specifically, 25 mg of freeze-dried nanoparticles were dispersed in 2.5 mL of an ethanolic solution of paracetamol (10 mg/mL) using an ultrasonic bath, followed by gentle stirring at room temperature for 2 h. After incubation, the suspension was centrifuged at 15000 rpm for 10 min. The resulting pellet was dried under a nitrogen stream, while the supernatant was collected for quantification of the unloaded paracetamol (free drug). The concentration of free paracetamol in the supernatant was determined by UV–Vis spectroscopy, using a Cary 3500 spectrophotometer (Agilent) and measuring absorbance at 243 nm. Prior to analysis, the supernatant was diluted 1:2500 in ultrapure water, and water was used as the blank. A calibration curve was established by measuring a series of paracetamol solutions prepared at defined concentrations in water.

The drug loading efficiency (LE%) and loading capacity (LC%) were calculated as follows:

$$LE\ (\%) = \frac{Initial\ drug - Free\ drug}{Initial\ drug} \cdot 100 \quad \text{(Equation 2)}$$

$$LC\ (\%) = \frac{Initial\ drug - Free\ drug}{Weight\ of\ nanoparticles} \cdot 100 \quad \text{(Equation 3)}$$

where *Initial drugs* is the amount (mg) of paracetamol initially present in the ethanolic solution, *Free drug* is the amount (mg) of unloaded drug, and *Weight of nanoparticles* refers to the mass (mg) of the freeze-dried nanoparticles used for the loading process.

To assess redispersion, the dried drug-loaded nanoparticles were redispersed in water using an ultrasonic bath and analyzed by DLS under the same conditions as the unloaded particles (0.5 mg/mL concentration).

For release experiments, 5 mg of paracetamol-loaded nanoparticles were dispersed in 5 mL of PBS buffer (pH 7.4) using an ultrasonic bath for 15 min to ensure homogeneous dispersion. The resulting suspension was then transferred into a dialysis membrane (cellulose dialysis tubing, average flat width 25 mm, Sigma-Aldrich), which was immersed in a test tube containing 5 mL of fresh PBS (pH 7.4). The entire system was maintained under continuous shaking at 37 °C to mimic physiological conditions. At predetermined time intervals (1 min, 5 min, 10 min, 15 min, 20 min, 30 min, 40 min, 60 min, 90 min, 120 min, 180 min), 0.5 mL aliquots were withdrawn from the external PBS medium and immediately replaced with an equal volume of fresh buffer to maintain sink conditions. The collected samples were analyzed by UV–Vis spectroscopy to determine the amount of paracetamol released over time.

3. Results and discussion

To optimize the experimental conditions for the synthesis of AMCP_PAA nanoparticles, we carried out a series of preliminary experiments, as detailed in the Supplementary Material (see Table S1–S4). These tests enabled us to identify the optimal synthetic conditions for AMCP_PAA nanoparticles. The final samples, listed in Table 3 with their respective nomenclatures, were thoroughly characterized and the results are outlined in the following sections.

3.1. Size and dispersibility of prepared particles

The size of the synthesized particles was characterized using DLS both during synthesis and after dispersion of the freeze-dried samples. To this purpose, we analyzed an aliquot of the colloidal dispersion collected after 1 h, as well as the lyophilized particles redispersed by means of two different types of sonication (see section 2.5). The normalized autocorrelation functions, along with the mean hydrodynamic diameters and the corresponding standard deviations, are provided in Fig. 1 and Table 4.

The results show that the presence of PAA promotes the formation of nanoparticles with a mean diameter in the range of several hundred nanometers and a polydispersity (PDI) of 0.2 or lower, indicating a relatively uniform distribution with some variability in particle sizes. In contrast, samples synthesized without PAA exhibited highly variable sizes exceeding 3 μm, likely due to spontaneous aggregation processes [2,12]. To better characterize the size distribution of AMCP prepared without PAA, laser granulometry experiments were carried out. The results, reported as D_{10}, D_{50} and D_{90}, show that particle diameters fall within the micrometer range, confirming the formation of large aggregates in the absence of the stabilizing effect of PAA (see Table S5).

The ability of PAA to dimensionally stabilize nanoparticles can be explained by its polymeric structure, which is rich in carboxylic groups

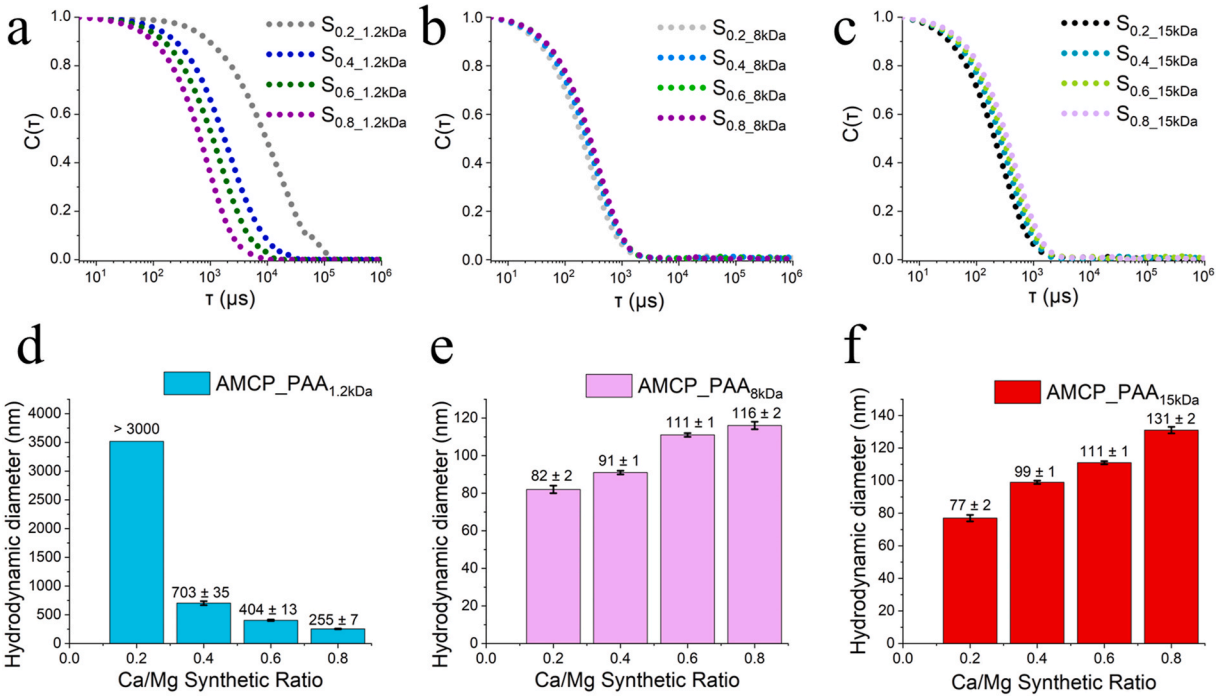

Fig. 1. Normalized autocorrelation functions (a, b, c) and mean hydrodynamic diameters with corresponding standard deviations (d, e, f) obtained from DLS measurements for the colloidal suspensions during synthesis (aliquot collected after 1 h). (a) and (d) AMCP_PAA$_{1.2\ kDa}$; (b) and (e) AMCP_PAA$_{8\ kDa}$; (c) and (f) AMCP_PAA$_{15\ kDa}$.

Table 4
Mean hydrodynamic diameters and polydispersity indices obtained from DLS measurements for the colloidal suspensions during synthesis and for the lyophilized powders redispersed (by ultrasonic bath or ultrasonic probe). Samples S_{Mg0}, $S_{0.2}$, $S_{0.4}$, $S_{0.6}$, and $S_{0.8}$ are omitted from this table due to their sizes exceeding 3 μm, beyond which DLS measurements become unreliable.

Sample	Colloidal Suspensions During Synthesis		Ultrasonic bath		Ultrasonic probe	
	Hydrodynamic Diameter (nm)	Polydispersity (PDI)	Hydrodynamic Diameter (nm)	Polydispersity (PDI)	Hydrodynamic Diameter (nm)	Polydispersity (PDI)
$S_{Mg0\_1.2kDa}$	129 ± 2	0.15 ± 0.02	260 ± 4	0.16 ± 0.03	200 ± 6	0.24 ± 0.02
$S_{0.8\_1.2kDa}$	255 ± 7	0.16 ± 0.02	187 ± 5	0.26 ± 0.02	173 ± 4	0.20 ± 0.03
$S_{0.6\_1.2kDa}$	404 ± 13	0.25 ± 0.03	232 ± 4	0.28 ± 0.01	189 ± 12	0.23 ± 0.02
$S_{0.4\_1.2kDa}$	703 ± 35	0.28 ± 0.04	207 ± 2	0.28 ± 0.03	203 ± 20	0.27 ± 0.03
$S_{0.2\_1.2kDa}$	>3000	0.40 ± 0.04	252 ± 24	0.24 ± 0.03	204 ± 18	0.21 ± 0.03
S_{Mg0_8kDa}	129 ± 1	0.21 ± 0.01	276 ± 21	0.14 ± 0.01	228 ± 5	0.21 ± 0.02
$S_{0.8\_8kDa}$	116 ± 2	0.15 ± 0.02	158 ± 2	0.22 ± 0.02	143 ± 7	0.20 ± 0.02
$S_{0.6\_8kDa}$	111 ± 1	0.16 ± 0.02	142 ± 2	0.19 ± 0.02	121 ± 5	0.21 ± 0.01
$S_{0.4\_8kDa}$	91 ± 1	0.20 ± 0.01	216 ± 6	0.25 ± 0.02	185 ± 23	0.22 ± 0.02
$S_{0.2\_8kDa}$	82 ± 2	0.22 ± 0.01	235 ± 5	0.28 ± 0.01	179 ± 12	0.19 ± 0.02
S_{Mg0_15kDa}	138 ± 1	0.17 ± 0.02	336 ± 7	0.27 ± 0.02	221 ± 8	0.25 ± 0.04
$S_{0.8\_15kDa}$	131 ± 2	0.17 ± 0.01	170 ± 12	0.19 ± 0.02	139 ± 3	0.26 ± 0.01
$S_{0.6\_15kDa}$	111 ± 1	0.13 ± 0.02	151 ± 2	0.18 ± 0.02	116 ± 3	0.20 ± 0.02
$S_{0.4\_15kDa}$	99 ± 1	0.19 ± 0.02	172 ± 3	0.20 ± 0.03	141 ± 4	0.17 ± 0.01
$S_{0.2\_15kDa}$	77 ± 2	0.20 ± 0.02	170 ± 2	0.20 ± 0.02	190 ± 15	0.22 ± 0.02

able to interact with the particle surfaces, providing steric stabilization. PAA's chelating properties enable the binding of metal ions such as calcium and magnesium, forming complexes that prevent particle growth and aggregation [26]. This limits agglomeration and ensures uniform size distribution.

In samples containing *PAA$_{8kDa}$* (Fig. 1b and e) and *PAA$_{15kDa}$* (Fig. 1c and f), we observed a reduction in the hydrodynamic diameter of the colloidal suspension with the decrease of Ca/Mg ratio, corresponding to an increase in magnesium content. Previous studies have reported that magnesium can influence the nucleation and growth of calcium phosphate phases, stabilizing amorphous intermediates, increasing solubility and affecting the crystallization process [59–61]. Our experimental results show that the particle size of both AMCP and AMCP_PAA decreases as Ca/Mg ratio decreases, possibly due to the role of magnesium ions during the initial stages of particle formation, where they may influence nucleation density and consequently limit particle growth.

In contrast, samples prepared with *PAA$_{1.2kDa}$* (Fig. 1a and d) exhibit the opposite behavior, with larger particle sizes as the magnesium content increases. These samples also display higher PDI values, ranging from approximately 0.3 to 0.4, indicating a broader size distribution and greater heterogeneity among the particles. We hypothesize that when using this type of PAA, the high amount of Mg^{2+} ions remaining in solution after AMCP formation interacts with the free carboxyl groups in PAA forming ionic "bridges" between particles and causing partial flocculation (see a sketch of the mechanism in Fig. S1). This interpretation is supported by the hydrodynamic diameter values obtained after redispersing the lyophilized powders by sonication, which are significantly smaller than during synthesis. This indicates that the structural

units are in the nanometer range for all AMCP_PAA samples, and the behavior of PAA 1.2 kDa reflects a reversible flocculation rather than true particle growth. This is reasonably due to its smaller M_w that provides less steric repulsion, thereby facilitating a faster flocculation process compared to the larger PAAs under investigation in this work.

Given that nanoparticles redispersibility is crucial in drug delivery to ensure uniform drug distribution, prevent aggregation, and maintain long-term stability thereby preserving the advantages of nanoscale dimensions, we measured the size of each sample after lyophilization and subsequent dispersion in Milli-Q water by two types of sonication (see section 2.5). As shown in Table 4, although most particles did not fully regain their original sizes, all samples recovered dimensions in the range of a few hundred nanometers, demonstrating excellent redispersion capability. Additionally, the PDI values for all dispersed samples ranged between 0.1 and 0.3. Notably, redispersion using a probe sonicator was more efficient than through an ultrasonic bath, yielding to dispersions with lower hydrodynamic diameters and requiring shorter sonication times.

3.2. Morphological and elemental characterization

The morphology of the synthesized particles was first examined using FE-SEM. As representative examples, the micrographs of $S_{0.8}$ and $S_{0.8\_8kDa}$ are shown in Fig. 2a and b, respectively, while a comprehensive overview of all samples is provided in Fig. S2–S4. Overall, both samples display similar morphologies characterized by highly disordered and aggregated structures, likely due to the lyophilization process. However, in certain regions of the sample, smaller and partially disaggregated structures can be observed (Fig. 2a and b); these are considered more representative of the PAA-containing particles in dispersion and are consistent with DLS measurements indicating particle sizes of hundreds of nanometers. Notably, such isolated particles are more frequently observed in the samples containing PAA compared to PAA-free samples such as $S_{0.8}$ which also shows individual objects in the nano range but is characterized by a DLS size exceeding 3 μm. This means that in solution the nanoparticles which compose the structural units of AMCPs undergo aggregation forming micrometric objects when no PAA is present in the synthetic medium.

EDS analysis confirmed the presence of Ca, Mg, P, and O elements in the particles. The elemental ratios are summarized in Table S6. As illustrated in Fig. 2c, the Ca/Mg ratio in the particles increases with the Ca/Mg ratio of the precursor salts used during the synthesis, in agreement with previously reported literature findings [26,33]. Although the Ca/Mg ratio in the final samples systematically varies with the synthesis conditions, it does not directly match the initial ratio used during synthesis. In fact, EDS shows that in all samples the Ca/Mg ratio in the final particles is higher than the one of the synthetic solutions, demonstrating a consistent preferential incorporation of calcium with respect to magnesium in AMCP particles. This evidence can be ascribed to two possible mechanisms taking place in our system, namely *i)* the higher affinity of PAA for calcium ions with respect to magnesium ions, which leads to a preferential interaction of PAA with calcium; *ii)* the higher solubility of magnesium phosphates with respect to calcium phosphates, which favor the precipitation of the latter [33,62,63]. We hypothesize that both factors contribute to the preferential incorporation of calcium over magnesium into the final products, which thus consists of ACP doped with Mg, with the amount of Mg in the final particles depending on the concentration of $MgCl_2$ relative to $CaCl_2$ in the synthetic solution. Both factors likely contributed to the preferential incorporation of calcium over magnesium into the final products.

To achieve a more detailed characterization of the samples' morphology, high-magnification BF-TEM micrographs were acquired. Fig. 3a and b show AMCP_PAA aggregates of different sizes, composed of small clusters of amorphous magnesium-calcium phosphate embedded within a PAA matrix. This suggests that the objects observed in DLS measurements do not consist of individual inorganic particles coated with a PAA layer, but are rather clusters of tens of nanometers in size, which aggregate to form larger structures. Furthermore, these results confirm that the unusually large particle sizes observed by DLS for the colloidal suspensions during synthesis in the $AMCP\_PAA_{1.2kDa}$ samples are likely due to a flocculation process, rather than representing individual particle sizes. EDS analysis coupled with TEM confirmed the previously observed trends (Table S7). The Selected Area Electron Diffraction (SAED) pattern (Fig. 3c and Fig. S5–S7) revealed the amorphous nature of the AMCP_PAA nanoparticles.

3.3. Structural and compositional characterization

Further investigations aimed at characterizing the structural nature (whether amorphous or crystalline) and the composition of the samples were carried out using FT-IR spectroscopy. Two main peaks relevant to phosphate crystallinity analysis can be identified: the first, located between 550 and 600 cm^{-1}, is attributed to the ν_4 asymmetric bending of the phosphate group, while the second, around 1000 cm^{-1}, corresponds to the ν_3 stretching mode of phosphate [33,64]. A key parameter for assessing the degree of crystallinity is the splitting of the peak associated with the ν_4 (asymmetric bending) vibration of phosphate [64]. The presence of split peaks in this region is indicative of a crystalline structure, whereas a single, broad peak suggests an amorphous phase.

The FT-IR spectra for the different samples are presented in Fig. 4 and Figure S8. Specifically, the spectra of magnesium-containing samples (AMCP and AMCP_PAA) exhibit characteristic signals of AMCP, whereas the spectra of magnesium-free samples (CP and CP_PAA) are consistent with HA [2,31–33,64–67]. A detailed peak assignment is provided in Table S8. These findings confirm the crucial role of magnesium in stabilizing the amorphous phase, in agreement with literature

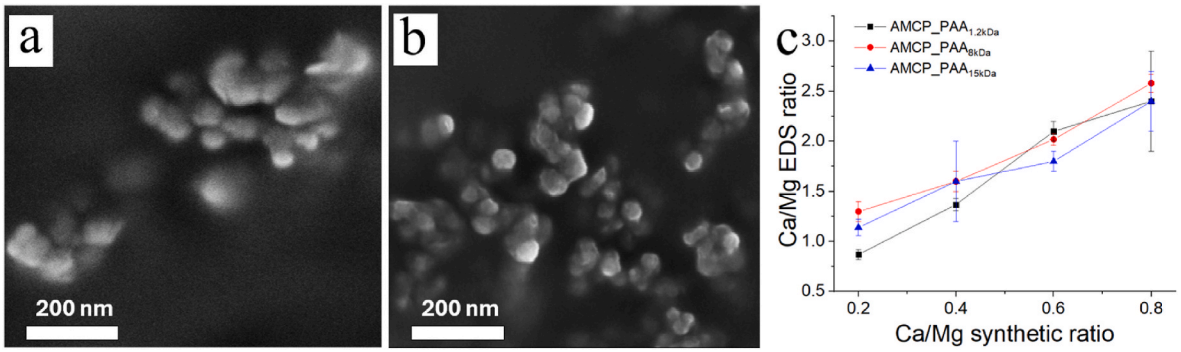

Fig. 2. FE-SEM micrograph of (a) $S_{0.8}$ as control, (b) $S_{0.8\_8kDa}$ representative of the morphology of all AMCP_PAA samples, and (c) plot of the semi-quantitative Ca/Mg atomic ratios obtained by SEM-EDS vs the Ca/Mg molar ratio used in the synthesis. The reported data are the average ± standard deviations of the values obtained in 3 different sites of each sample.

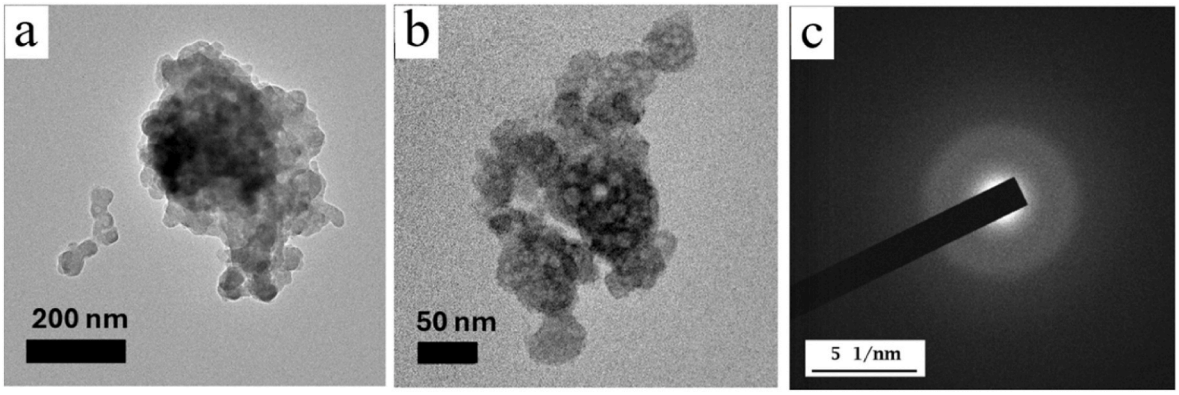

Fig. 3. (a and b) BF-TEM micrographs, and (c) SAED pattern of AMCP_PAA samples. The images presented correspond to the $S_{0.8\_8kDa}$ sample, which is representative of the morphology of all other samples. Detailed micrographs of all samples can be found in the Supplementary Material (Fig. S5–S7).

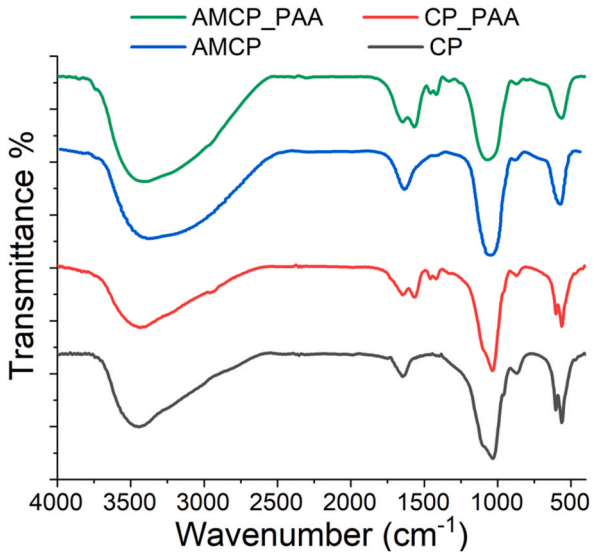

Fig. 4. FT-IR spectra of CP particles (black curve, corresponding to sample S_{Mg0}); CP_PAA (red curve, corresponding to sample S_{Mg0_8kDa}); AMCP (blue curve, corresponding to sample $S_{0.8}$); and AMCP_PAA (green curve, corresponding to sample $S_{0.8\_8kDa}$). The spectra are offset along the y axis for display purposes.

data [32,33]. Additionally, the incorporation of PAA into the CP_PAA and AMCP_PAA samples is demonstrated by the presence of additional signals corresponding to PAA molecules, which are not observed in the control samples prepared without PAA (*i.e.* $S_{0.2}$, $S_{0.4}$, $S_{0.6}$, $S_{0.8}$ and S_{Mg0}). It is well known that PAA is able to chelate Ca^{2+} ions [68–70] and, to a lesser extent, Mg^{2+} [71,72]. Following the chelation of PAA with Ca^{2+} ions, the C=O and C–O stretching vibrations become strongly coupled, leading to characteristic peaks associated with carboxylate (COO^-) stretching, observed around ~1560 cm^{-1} (see Fig. S9) [26]. Furthermore, additional signals characteristic of long carbon chains can be identified, particularly a band at approximately 1460 cm^{-1}, which is attributed to CH_2 scissor vibrations near the carboxyl group [73].

To confirm the structural features suggested by FT-IR, and SAED analysis, XRD measurements were also carried out (Fig. S10). The diffraction patterns confirmed the amorphous nature of AMCP and AMCP_PAA samples. In contrast, CP samples exhibited diffraction patterns characteristic of nano hydroxyapatite [74].

3.4. Thermal behavior and PAA quantification

The analysis of thermal degradation and heat flow profiles provides insights into the properties of the particles. The thermogram of AMCP (Fig. 5a) reveals that degradation occurs in three distinct stages: an initial loss of loosely bound water between 30 and 140 °C, followed by the release of strongly bound internal water from 140 to 560 °C, and finally, a weight loss associated with the crystallization process between 560 and 680 °C, consistently with previous studies [33]. The inorganic nature of AMCP results in a residual mass between 72 and 75 % at 1000 °C, depending on Ca/Mg. In contrast, AMCP_PAA exhibits a lower residual mass (69–65 %) due to the presence of PAA. The thermal decomposition of PAA (solution at 35–45 wt%) occurs in multiple stages: first, the evaporation of the water in solution between 30 and 80 °C, followed by dehydration and the formation of PAA anhydride from 80 to 200 °C [75,76]. These events are followed by the degradation of the PAA anhydride between 200 and 500 °C, with CO_2 release and the formation of a cyclic ketone, which further decomposes with CO loss [75,76]. Finally, the degradation of the PAA backbone occurs between 600 and 900 °C.

The PAA content in the different samples can be quantified by analyzing the residual mass of AMCP_PAA, AMCP, and PAA. The latter is corrected for the weight loss due to water evaporation, as we tested a 35–45 wt% solution rather than a pure polymer. The corresponding results (±1 %, instrumental uncertainty) for each sample are presented in Fig. 5b and summarized in Table S9, while the thermograms of all samples are provided in Figs. S11–S14 in the Supplementary Material. A trend in polymer content as a function of the Ca/Mg synthetic molar ratio can be observed, showing an overall increase in PAA content with the decrease in Mg concentration, which suggests a greater affinity of the polymer for calcium ions compared to magnesium ions.

Crystallization of ACP and AMCP is typically observed as an exothermic signal in the heat flow profiles of the Differential Scanning Calorimetry curves [33,77–79]. The temperature at which crystallization occurs provides information about the thermal stability of the amorphous phase. In our case the heat flow profiles shown in Fig. 6 indicate that amorphous particles crystallize at temperatures ranging from 641 °C to 725 °C. All samples exhibit a single crystallization peak, except for $S_{0.4}$, $S_{0.6}$, $S_{0.8}$, $S_{0.4\_1.2kDa}$, $S_{0.6\_1.2kDa}$, and $S_{0.8\_1.2kDa}$, which undergo crystallization in two distinct steps.

Literature reports [33] suggest that an increase in magnesium content in the particles delays the thermal crystallization of AMCP. However, our results do not reveal any significant change in the crystallization temperature with varying magnesium levels. Interestingly, a stabilizing effect of PAA is consistently observed, as all PAA-containing samples exhibit higher crystallization temperatures compared to those without PAA, at the same Ca/Mg ratio. This effect is particularly pronounced in samples with PAA_{8kDa} and PAA_{15kDa}, which show the highest crystallization temperatures (Fig. 7).

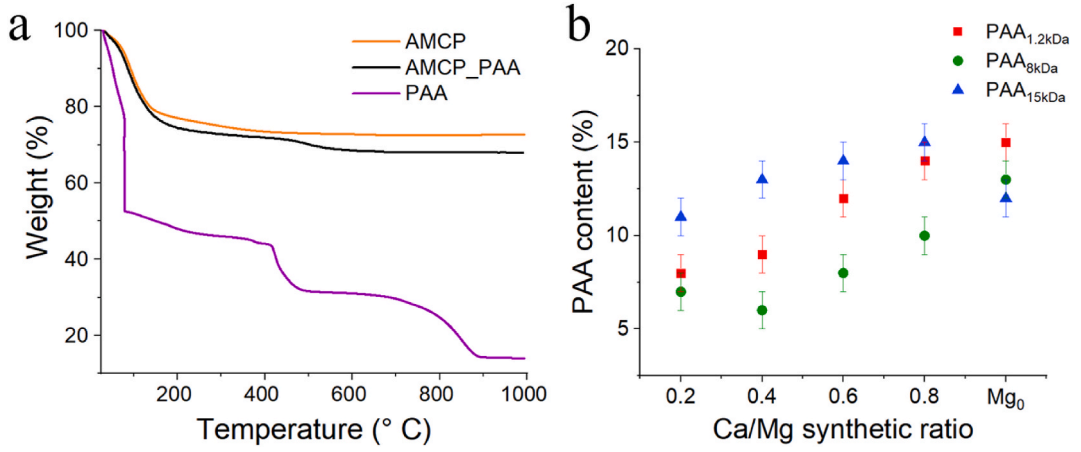

Fig. 5. (a) Thermograms of AMCP_PAA (black curve, sample $S_{0.8\_8kDa}$) compared to pure AMCP (orange curve, sample $S_{0.8}$) and PAA (purple curve, PAA_{8kDa}); The PAA solution was treated using a three-stage procedure to ensure complete water evaporation: an initial heating ramp from room temperature to 80 °C (10 °C/min), followed by equilibration at 80 °C for 30 min. (b) Variation of PAA content in the prepared samples (± instrumental uncertainty) as a function of the Ca/Mg synthetic molar ratio, determined through TGA analysis.

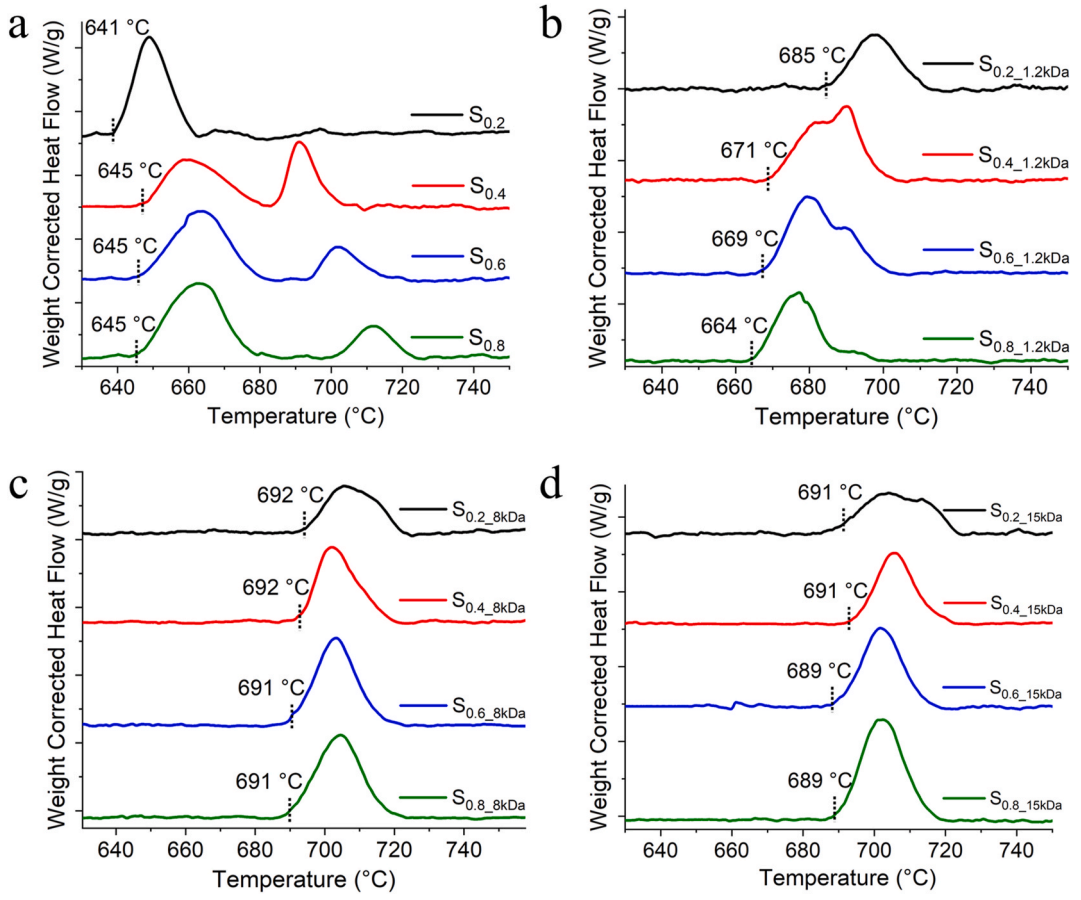

Fig. 6. Weight corrected heat flow profiles (exo up) of (a) AMCP, (b) $AMCP\_PAA_{1.2kDa}$, (c) $AMCP\_PAA_{8kDa}$, and (d) $AMCP\_PAA_{15kDa}$. The curves are offset along the y axis for display purposes.

3.5. Stability assessment

Studying the stability of CP nanoparticles in buffer solutions at different pH values is crucial for their application in drug delivery. In physiological conditions (pH ~7.4), nanoparticles should remain stable to ensure effective circulation and targeted delivery. However, under acidic conditions (pH ~5), such as those found in intracellular compartments like endosomes and lysosomes, as well as in the tumor microenvironment, nanoparticles may undergo controlled dissolution, facilitating drug release at the desired site. The ability to fine-tune nanoparticle stability in response to pH variations is essential for optimizing their performance in targeted therapies, minimizing premature degradation, and enhancing drug bioavailability.

Stability tests were carried out on AMCP, $AMCP\_PAA_{8kDa}$ series,

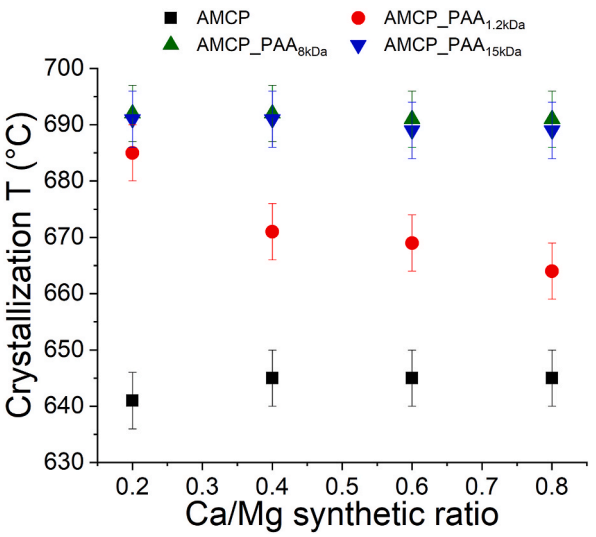

Fig. 7. Plot of the crystallization T (peak onset) ± standard deviation (calculated considering three replicates) vs the Ca/Mg synthetic ratio.

$S_{0.8\_1.2kDa}$ and $S_{0.8\_15kDa}$ samples to assess potential differences related to Ca/Mg ratio or, for samples with the same magnesium content, the effect of PAA molecular weight. Samples were incubated in buffer solutions at different pH as detailed in section 2.6, then recovered by means of centrifugation and freeze-drying, and finally analyzed by means of FT-IR spectroscopy. Results (see Fig. 8a) show that PAA-containing samples remain stable at least for five days in PBS buffer (pH 7.4), regardless of PAA type or magnesium content.

In contrast, AMCP samples without PAA undergo conversion to HA (Fig. 8a and Figure S15), with the transformation rate depending on magnesium content. Sample $S_{0.2}$, which has the highest magnesium content, remains stable in its amorphous form throughout the investigated period. This observation underscores the stabilizing role of PAA in preventing the crystallization of AMCP in solution, aligning with existing literature on its ability to preserve the amorphous form [26,46]. However, while previous studies have primarily focused on the thermal stability of AMCP [26,46], our findings provide new insights by demonstrating the stabilizing effect of PAA in solution, offering a complementary perspective on its role in maintaining AMCP in the amorphous state. The stabilizing activity of PAA can be explained by its ability to chelate Ca^{2+} ions, leading to the formation of more stable PAA-AMCP complexes that may dissolve more slowly, thereby slowing down the crystallization process, helpings the preservation of the amorphous phase. An additional intriguing result was observed for PAA-containing samples dispersed in acetate buffer (pH 5). While AMCP samples without PAA were completely dissolved after less that 2 min of incubation, PAA-containing samples retained a visible precipitate for at least the first 5 min (Fig. S16a), with the $S_{0.8\_8kDa}$ sample exhibiting maximum stability by retaining a visibile precipitate for 15 min. The collected pellet from the $S_{0.8\_8kDa}$ sample was analyzed via FT-IR, and the resulting spectrum (Fig. 8b) confirmed that the presence of PAA endows AMCP with partial resistance to dissolution in acidic conditions while still allowing their pH-responsiveness in acidic environment: in fact, after 15 min of incubation in acetate buffer, no visible solid was observed. Nevertheless, DLS measurements (autocorrelection function shown in Fig. S16b) conducted after 30 min revealed the presence of nanometric objects (mean diameter of (292 ± 15) nm and polydispersity of 0.17 ± 0.03), which may correspond either to partially dissolved nanoparticles or to complexes formed in solution between PAA and calcium ions. Notably, it was not possible to collect these objects by centrifugation, suggesting that they are more likely calcium-PAA complexes rather than residual nanoparticles.

The pH responsiveness of PAA is well-documented in the literature [80,81]. PAA is an anionic polymer whose conformation and properties are strongly influenced by the pH of the surrounding solution due to the presence of carboxyl (-COOH) groups along its backbone. At pH values below its pKa (~5–6), the carboxyl groups remain predominantly protonated (-COOH), reducing electrostatic repulsions between polymer chains and promoting intermolecular interactions through hydrogen bonding among the carboxyl groups. This leads to a conformational collapse of the polymer structure. Conversely, when the pH exceeds the pKa of PAA, the carboxyl groups undergo deprotonation ($-COO^-$), imparting a negative charge to the polymer. The resulting increase in electrostatic repulsion between the $-COO^-$ groups along the chain induces a conformational transition toward an expanded structure (swelling effect). This delayed dissolution in acidic environments can be advantageous in drug delivery applications. A gradual dissolution of the

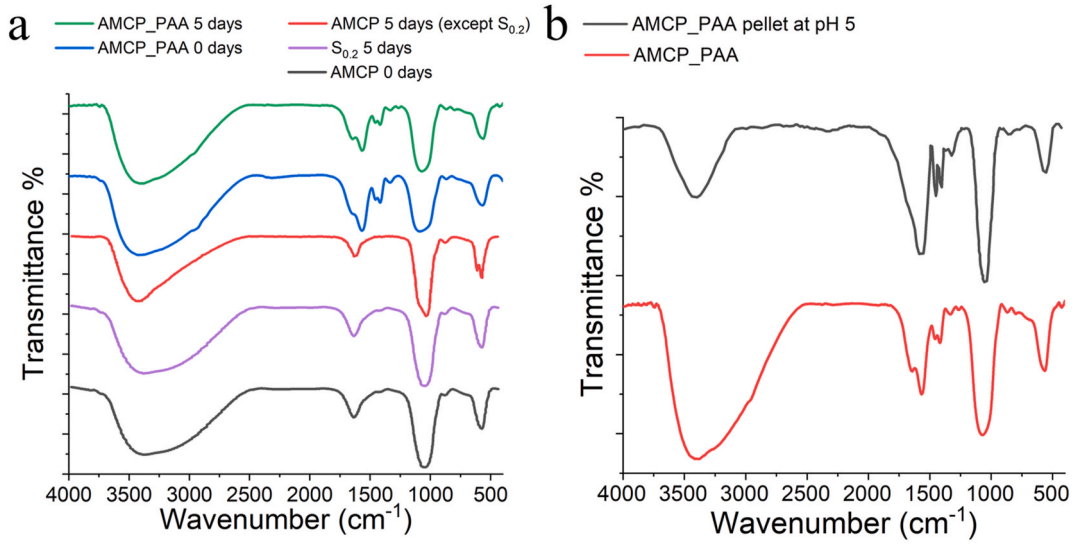

Fig. 8. (a) FT-IR spectrum of freshly prepared AMCP (black curve, $S_{0.2}$ representative of all AMCP samples), $S_{0.2}$ pellet after dispersion in PBS buffer at pH 7.4 for 5 days (purple curve), AMCP pellet after 5 days (red curve, $S_{0.8}$ representative of all AMCP samples except $S_{0.2}$) consistent with the presence of HA, freshly prepared AMCP_PAA (blue curve, $S_{0.8\_8kDa}$ representative of all AMCP_PAA samples), and AMCP_PAA pellet after dispersion in PBS buffer at pH 7.4 for 5 d (green curve, $S_{0.8\_8kDa}$ representative of all AMCP_PAA samples). (b) FT-IR spectrum of the recovered AMCP_PAA pellet after at least 5 min of incubation in acetate buffer at pH 5 (black curve) compared to freshly prepared AMCP_PAA (red curve). Both spectra correspond to the $S_{0.8\_8kDa}$ sample, which is presented as a representative example.

nanoparticles might enable a more controlled release of encapsulated drugs, potentially enhancing therapeutic efficacy. This feature is particularly beneficial for targeted drug delivery to tumor tissues or intracellular compartments, where a controlled and gradual release can improve treatment effectiveness [82,83].

3.6. Drug loading and release behavior

To demonstrate the applicability of AMCP_PAA nanoparticles as drug carriers, a representative sample ($S_{0.8\_15kDa}$) was loaded with paracetamol and evaluated in terms of redispersion and release performance. UV–Vis quantification of the unbound drug allowed for the calculation of drug loading efficiency (LE%) and loading capacity (LC%), both found to be approximately 20 %, confirming the effective incorporation of paracetamol into the nanoparticle.

Redispersion tests revealed that the drug-loaded nanoparticles retained excellent colloidal properties, with hydrodynamic diameter comparable to that of the unloaded sample (Fig. S17a). Furthermore, a preliminary release experiment performed under physiological conditions (PBS, pH 7.4, 37 °C) demonstrated the ability to release paracetamol, with a maximum of approximately 10 % of cumulative release after 3 h of incubation (Fig. S17b). Although a comprehensive evaluation of the drug release kinetics falls outside the scope of this work, these preliminary results provide a first indication of the nanoparticles' ability to load and release a model drug, supporting their potential for future drug delivery applications.

4. Conclusions

This study provides a comprehensive investigation of the synthesis, characterization, and stability of AMCP_PAA nanoparticles, with a particular focus on the influence of PAA molecular weight and the relative calcium-magnesium content in the nanoparticles. The findings highlight the crucial role of PAA in stabilizing AMCP nanoparticles, as evidenced by the significantly reduced particle aggregation and improved size uniformity compared to PAA-free samples. A major contribution of this work is its focus on the redispersibility of nanoparticles after freeze-drying, an aspect often overlooked in previous studies [17,26,27,30,55]. While most existing research focuses on particle size during synthesis, we show that PAA-stabilized AMCP nanoparticles maintain their nanoscale size upon redispersion, with diameters of few hundred nanometers. Additionally, we compared two sonication methods using a probe sonicator and a bath sonicator, finding that the probe sonicator was more efficient, producing dispersions with smaller hydrodynamic diameters and requiring less sonication time. This feature is critical for practical applications, as nanoparticles are often dried and reconstituted before use in biomedical settings. Furthermore, this study explores, for the first time, how different combinations of Ca/Mg ratios in AMCP and varying PAA molecular weights influence the stability, dispersibility, and crystallization of the nanoparticles. While previous studies have primarily focused on the thermal stability of AMCP [26,46], our work investigates not only its thermal stability but also its stability in aqueous environments, a fundamental aspect for biomedical applications.

The structural and compositional analyses performed via FT-IR and thermal analysis demonstrated that magnesium plays a key role in delaying the thermal crystallization of AMCP, in agreement with literature reports [26,46]. Additionally, PAA further stabilizes the amorphous phase by chelating calcium ions, thereby preventing premature crystallization.

Stability assessments in physiologically relevant conditions revealed that PAA-containing AMCP nanoparticles remain stable in PBS (pH 7.4), preventing conversion to HA, whereas PAA-free AMCP undergoes transformation within 5 days except for $S_{0.2}$ which exhibits remarkable stability due to its higher magnesium content. Furthermore, incubation in acidic conditions (pH 5) induced a more gradual dissolution of PAA-containing samples, suggesting pH-responsive behavior that may be beneficial for targeted drug delivery applications. The delayed dissolution effect, attributed to PAA's pH-dependent conformational changes [80,81], offers potential advantages for controlled drug release in acidic environments such as tumor microenvironments or intracellular compartments. Future studies will focus on a more quantitative analysis of the dissolution kinetics of AMCP, in the presence and absence of PAA.

Overall, these findings underscore the significance of both PAA molecular weight and magnesium content in tuning the stability and crystallization behavior of AMCP nanoparticles. The ability to tailor these parameters offers promising prospects for the development of stable, pH-responsive nanosystems for biomedical applications, particularly in drug delivery. Future studies will focus on optimizing these formulations for specific therapeutic applications and evaluating their *in vitro* and *in vivo* performance [82,83].

CRediT authorship contribution statement

Debora Briganti: Writing – original draft, Visualization, Investigation, Formal analysis, Conceptualization. **Melissa Saibene:** Writing – review & editing, Investigation, Formal analysis. **Giancarlo Capitani:** Writing – review & editing, Investigation. **Rita Gelli:** Writing – review & editing, Supervision, Formal analysis, Conceptualization. **Francesca Ridi:** Writing – review & editing, Supervision, Project administration, Funding acquisition, Conceptualization.

Funding

This work was supported by the Plantform project, n° F/310143/01–03/X56, "Accordo per l'innovazione 18/10/2023", Ministry of Enterprise and Made in Italy. CSGI (Consorzio Interuniversitario per lo Sviluppo dei Sistemi a Grande Interfase) and MUR-Italy ("Progetto Dipartimenti di Eccellenza 2023–2027" 58503DIP_ECC allocated to Department of Chemistry "Ugo Schiff") are also acknowledged for the financial support. The authors gratefully acknowledge the support of the ISIS@MACH ITALIA Research Infrastructure, the hub of ISIS Neutron and Muon Source (UK), MUR official registry U. 0008642.28-05-2020 –16th April 2020.

Declaration of competing interest

The authors declare that they have no known competing financial interests or personal relationships that could have appeared to influence the work reported in this paper.

Appendix A. Supplementary data

Supplementary data to this article can be found online at https://doi.org/10.1016/j.mtnano.2025.100655.

Data availability

Data will be made available on request.

References

[1] S.V. Dorozhkin, Calcium orthophosphates in nature, biology and medicine, Materials 2 (2009) 399–498, https://doi.org/10.3390/ma2020399.
[2] R. Gelli, F. Ridi, P. Baglioni, The importance of being amorphous: calcium and magnesium phosphates in the human body, Adv. Colloid Interface Sci. 269 (2019) 219–235, https://doi.org/10.1016/j.cis.2019.04.011.
[3] E. Boanini, M. Gazzano, A. Bigi, Ionic substitutions in calcium phosphates synthesized at low temperature, Acta Biomater. 6 (2010) 1882–1894, https://doi.org/10.1016/j.actbio.2009.12.041.
[4] T.J. Levingstone, S. Herbaj, N.J. Dunne, Calcium phosphate nanoparticles for therapeutic applications in bone regeneration, Nanomaterials 9 (2019), https://doi.org/10.3390/nano9111570.
[5] L.-H. Fu, Y.-R. Hu, C. Qi, T. He, S. Jiang, C. Jiang, J. He, J. Qu, J. Lin, P. Huang, Biodegradable manganese-doped calcium phosphate nanotheranostics for

traceable cascade reaction-enhanced anti-tumor therapy, ACS Nano 13 (2019) 13985–13994, https://doi.org/10.1021/acsnano.9b05836.
[6] Y. Xiao, Z. Li, A. Bianco, B. Ma, Recent advances in calcium-based anticancer nanomaterials exploiting calcium overload to trigger cell apoptosis, Adv. Funct. Mater. 33 (2023) 2209291, https://doi.org/10.1002/adfm.202209291.
[7] C. Wang, J. Peng, Y. Xiao, Z. Zhang, X. Yang, X. Liang, J. Yang, X. Zhou, C. Li, Advances in nanotherapeutics for tumor treatment by targeting calcium overload, Colloids Surf. B Biointerfaces 245 (2025) 114190, https://doi.org/10.1016/j.colsurfb.2024.114190.
[8] P. Liu, J. Guo, Z. Xie, Y. Pan, B. Wei, Y. Peng, S. Hu, J. Ding, X. Chen, J. Su, H. Liu, W. Zhou, Co-delivery of aPD-L1 and CD73 inhibitor using calcium phosphate nanoparticles for enhanced melanoma immunotherapy with reduced toxicity, Adv. Sci. 12 (2025) 2410545, https://doi.org/10.1002/advs.202410545.
[9] Y. Xiao, J. Lin, Y. Zhao, X. Wang, Q. Lv, W. Li, R. Tang, G. Fu, Plaque-specific adhesive balloons coated with calcium phosphate nanoparticles loaded with rapamycin for atherosclerosis therapy, Adv. Funct. Mater. 34 (2024) 2315317, https://doi.org/10.1002/adfm.202315317.
[10] Z. Xing, S. Chen, Z. Liu, X. Yang, X. Zhu, X. Zhang, Harnessing the power of hydroxyapatite nanoparticles for gene therapy, Appl. Mater. Today 39 (2024) 102317, https://doi.org/10.1016/j.apmt.2024.102317.
[11] Z. Sun, W. Li, J.C. Lenzo, J.A. Holden, M.J. McCullough, A.J. O'Connor, N. M. O'Brien-Simpson, The potential of calcium phosphate nanoparticles as adjuvants and vaccine delivery vehicles, Front. Mater. 8 (2021), https://doi.org/10.3389/fmats.2021.788373.
[12] J.J. Powell, E. Thomas-McKay, V. Thoree, J. Robertson, R.E. Hewitt, J.N. Skepper, A. Brown, J.C. Hernandez-Garrido, P.A. Midgley, I. Gomez-Morilla, G.W. Grime, K. J. Kirkby, N.A. Mabbott, D.S. Donaldson, I.R. Williams, D. Rios, S.E. Girardin, C. T. Haas, S.F.A. Bruggraber, J.D. Laman, Y. Tanriver, G. Lombardi, R. Lechler, R.P. H. Thompson, L.C. Pele, An endogenous nanomineral chaperones luminal antigen and peptidoglycan to intestinal immune cells, Nat. Nanotechnol. 10 (2015) 361–369, https://doi.org/10.1038/nnano.2015.19.
[13] Y. Li, T. Wiliana, K.C. Tam, Synthesis of amorphous calcium phosphate using various types of cyclodextrins, Mater. Res. Bull. 42 (2007) 820–827, https://doi.org/10.1016/j.materresbull.2006.08.027.
[14] M.-G. Ma, Y.-J. Zhu, J. Chang, Monetite formed in mixed solvents of water and ethylene glycol and its transformation to hydroxyapatite, J. Phys. Chem. B 110 (2006) 14226–14230, https://doi.org/10.1021/jp061738r.
[15] L.B. Gower, Biomimetic model systems for investigating the amorphous precursor pathway and its role in biomineralization, Chem. Rev. 108 (2008) 4551–4627, https://doi.org/10.1021/cr800443h.
[16] S. Boonrungsiman, E. Gentleman, R. Carzaniga, N.D. Evans, D.W. McComb, A. E. Porter, M.M. Stevens, The role of intracellular calcium phosphate in osteoblast-mediated bone apatite formation, Proc. Natl. Acad. Sci. 109 (2012) 14170–14175, https://doi.org/10.1073/pnas.1208916109.
[17] R.-H. Lai, P.-J. Dong, Y.-L. Wang, J.-B. Luo, Redispersible and stable amorphous calcium phosphate nanoparticles functionalized by an organic bisphosphate, Chin. Chem. Lett. 25 (2014) 295–298, https://doi.org/10.1016/j.cclet.2013.11.012.
[18] K. Öztürk, M. Kaplan, S. Çalış, Effects of nanoparticle size, shape, and zeta potential on drug delivery, Int. J. Pharm. 666 (2024) 124799, https://doi.org/10.1016/j.ijpharm.2024.124799.
[19] M.J. Mitchell, M.M. Billingsley, R.M. Haley, M.E. Wechsler, N.A. Peppas, R. Langer, Engineering precision nanoparticles for drug delivery, Nat. Rev. Drug Discov. 20 (2021) 101–124, https://doi.org/10.1038/s41573-020-0090-8.
[20] S. Guo, Y. Liang, L. Liu, M. Yin, A. Wang, K. Sun, Y. Li, Y. Shi, Research on the fate of polymeric nanoparticles in the process of the intestinal absorption based on model nanoparticles with various characteristics: size, surface charge and pro-hydrophobics, J. Nanobiotechnol. 19 (2021) 32, https://doi.org/10.1186/s12951-021-00770-2.
[21] A. Dey, P.H.H. Bomans, F.A. Müller, J. Will, P.M. Frederik, G. de With, N.A.J. M. Sommerdijk, The role of prenucleation clusters in surface-induced calcium phosphate crystallization, Nat. Mater. 9 (2010) 1010–1014, https://doi.org/10.1038/nmat2900.
[22] V. Čadež, I. Erceg, A. Selmani, D. Domazet Jurašin, S. Šegota, D.M. Lyons, D. Kralj, M.D. Sikirić, Amorphous calcium phosphate formation and aggregation process revealed by light scattering techniques, Crystals 8 (2018) 254, https://doi.org/10.3390/cryst8060254.
[23] S. Jiang, W. Jin, Y.-N. Wang, H. Pan, Z. Sun, R. Tang, Effect of the aggregation state of amorphous calcium phosphate on hydroxyapatite nucleation kinetics, RSC Adv. 7 (2017) 25497–25503, https://doi.org/10.1039/C7RA02208E.
[24] S.V. Dorozhkin, Calcium orthophosphates (CaPO4): occurrence and properties, Prog. Biomater. 5 (2016) 9–70, https://doi.org/10.1007/s40204-015-0045-z.
[25] S.V. Dorozhkin, Synthetic amorphous calcium phosphates (ACPs): preparation, structure, properties, and biomedical applications, Biomater. Sci. 9 (2021) 7748–7798, https://doi.org/10.1039/D1BM01239H.
[26] N. Li, W. Cui, P. Cong, J. Tang, Y. Guan, C. Huang, Y. Liu, C. Yu, R. Yang, X. Zhang, Biomimetic inorganic-organic hybrid nanoparticles from magnesium-substituted amorphous calcium phosphate clusters and polyacrylic acid molecules, Bioact. Mater. 6 (2021) 2303–2314, https://doi.org/10.1016/j.bioactmat.2021.01.005.
[27] B. Sun, M. Gillard, Y. Wu, P. Wu, Z.P. Xu, W. Gu, Bisphosphonate stabilized calcium phosphate nanoparticles for effective delivery of plasmid DNA to macrophages, ACS Appl. Bio Mater. 3 (2020) 986–996, https://doi.org/10.1021/acsabm.9b00994.
[28] K. Asai, N. Kanayama, Y. Nagasaki, Preparation and evaluation of highly dispersible and Ca2+ level responsive PEGylated calcium phosphate nanoparticle with PEG-block-poly(4-vinylbenzylphosphonate) for the application of drug carrier, Trans. Mater. Res. Soc. Jpn. 37 (2012) 337–340, https://doi.org/10.14723/tmrsj.37.337.
[29] S. Bisso, S. Mura, B. Castagner, P. Couvreur, J.-C. Leroux, Dual delivery of nucleic acids and PEGylated-bisphosphonates via calcium phosphate nanoparticles, Eur. J. Pharm. Biopharm. 142 (2019) 142–152, https://doi.org/10.1016/j.ejpb.2019.06.013.
[30] E.V. Giger, J. Puigmartí-Luis, R. Schlatter, B. Castagner, P.S. Dittrich, J.-C. Leroux, Gene delivery with bisphosphonate-stabilized calcium phosphate nanoparticles, J. Contr. Release 150 (2011) 87–93, https://doi.org/10.1016/j.jconrel.2010.11.012.
[31] R. Gelli, S. Salvestrini, F. Ridi, Effect of biologically-relevant molecules on the physico-chemical properties of amorphous magnesium–calcium phosphate nanoparticles, J. Nanosci. Nanotechnol. 21 (2021) 2872–2878, https://doi.org/10.1166/jnn.2021.19049.
[32] R. Gelli, M. Scudero, L. Gigli, M. Severi, M. Bonini, F. Ridi, P. Baglioni, Effect of pH and Mg2+ on amorphous magnesium-calcium phosphate (AMCP) stability, J. Colloid Interface Sci. 531 (2018) 681–692, https://doi.org/10.1016/j.jcis.2018.07.102.
[33] R. Gelli, L. Briccolani-Bandini, M. Pagliai, G. Cardini, F. Ridi, P. Baglioni, Exploring the effect of Mg^{2+} substitution on amorphous calcium phosphate nanoparticles, J. Colloid Interface Sci. 606 (2022) 444–453, https://doi.org/10.1016/j.jcis.2021.08.033.
[34] H. Song, M. Cai, Z. Fu, Z. Zou, Mineralization pathways of amorphous calcium phosphate in the presence of fluoride, Cryst. Growth Des. 23 (2023) 7150–7158, https://doi.org/10.1021/acs.cgd.3c00541.
[35] Y. Chen, W. Gu, H. Pan, S. Jiang, R. Tang, Stabilizing amorphous calcium phosphate phase by citrate adsorption, CrystEngComm 16 (2014) 1864–1867, https://doi.org/10.1039/C3CE42274G.
[36] E. Ruiz-Agudo, C. Ruiz-Agudo, F. Di Lorenzo, P. Alvarez-Lloret, A. Ibañez-Velasco, C. Rodriguez-Navarro, Citrate stabilizes hydroxylapatite precursors: implications for bone mineralization, ACS Biomater. Sci. Eng. 7 (2021) 2346–2357, https://doi.org/10.1021/acsbiomaterials.1c00196.
[37] R. Gelli, V. Pucci, F. Ridi, P. Baglioni, A study on biorelevant calciprotein particles: effect of stabilizing agents on the formation and crystallization mechanisms, J. Colloid Interface Sci. 620 (2022) 431–441, https://doi.org/10.1016/j.jcis.2022.04.025.
[38] L. Degli Esposti, A. Adamiano, A. Tampieri, G.B. Ramirez-Rodriguez, D. Siliqi, C. Giannini, P. Ivanchenko, G. Martra, F.-H. Lin, J.M. Delgado-López, M. Iafisco, Combined effect of citrate and fluoride ions on hydroxyapatite nanoparticles, Cryst. Growth Des. 20 (2020) 3163–3172, https://doi.org/10.1021/acs.cgd.0c00038.
[39] L.D. Esposti, S. Markovic, N. Ignjatovic, S. Panseri, M. Montesi, A. Adamiano, M. Fosca, J.V. Rau, V. Uskoković, M. Iafisco, Thermal crystallization of amorphous calcium phosphate combined with citrate and fluoride doping: a novel route to produce hydroxyapatite bioceramics, J. Mater. Chem. B 9 (2021) 4832–4845, https://doi.org/10.1039/D1TB00601K.
[40] M. Iafisco, L. Degli Esposti, G.B. Ramírez-Rodríguez, F. Carella, J. Gómez-Morales, A.C. Ionescu, E. Brambilla, A. Tampieri, J.M. Delgado-López, Fluoride-doped amorphous calcium phosphate nanoparticles as a promising biomimetic material for dental remineralization, Sci. Rep. 8 (2018) 17016, https://doi.org/10.1038/s41598-018-35258-x.
[41] J. Santiago-Morales, G. Amariei, P. Letón, R. Rosal, Antimicrobial activity of poly (vinyl alcohol)-poly(acrylic acid) electrospun nanofibers, Colloids Surf. B Biointerfaces 146 (2016) 144–151, https://doi.org/10.1016/j.colsurfb.2016.04.052.
[42] P. Ghaffari-Bohlouli, P. Zahedi, M. Shahrousvand, Enhanced osteogenesis using poly (l-lactide-co-d, l-lactide)/poly (acrylic acid) nanofibrous scaffolds in presence of dexamethasone-loaded molecularly imprinted polymer nanoparticles, Int. J. Biol. Macromol. 165 (2020) 2363–2377, https://doi.org/10.1016/j.ijbiomac.2020.10.078.
[43] N. Bagheri, M. Mansour Lakouraj, S.R. Nabavi, H. Tashakkorian, M. Mohseni, Synthesis of bioactive polyaniline- *b* -polyacrylic acid copolymer nanofibrils as an effective antibacterial and anticancer agent in cancer therapy, especially for HT29 treatment, RSC Adv. 10 (2020) 25290–25304, https://doi.org/10.1039/D0RA03779F.
[44] H. Arkaban, M. Barani, M.R. Akbarizadeh, N. Pal Singh Chauhan, S. Jadoun, M. Dehghani Soltani, P. Zarrintaj, Polyacrylic acid nanoplatforms: antimicrobial, tissue engineering, and cancer theranostic applications, Polymers 14 (2022) 1259, https://doi.org/10.3390/polym14061259.
[45] H. Shi, L. Li, L. Zhang, T. Wang, C. Wang, D. Zhu, Z. Su, Designed preparation of polyacrylic acid/calcium carbonate nanoparticles with high doxorubicin payload for liver cancer chemotherapy, CrystEngComm 17 (2015) 4768–4773, https://doi.org/10.1039/C5CE00708A.
[46] S.-C. Huang, K. Naka, Y. Chujo, A carbonate controlled-addition method for amorphous calcium carbonate spheres stabilized by poly(acrylic acid)s, Langmuir 23 (2007) 12086–12095, https://doi.org/10.1021/la701972n.
[47] G.-B. Cai, G.-X. Zhao, X.-K. Wang, S.-H. Yu, Synthesis of polyacrylic acid stabilized amorphous calcium carbonate nanoparticles and their application for removal of toxic heavy metal ions in water, J. Phys. Chem. C 114 (2010) 12948–12954, https://doi.org/10.1021/jp103464p.
[48] C. Xu, Y. Yan, J. Tan, D. Yang, X. Jia, L. Wang, Y. Xu, S. Cao, S. Sun, Biodegradable nanoparticles of polyacrylic acid–stabilized amorphous $CaCO_3$ for tunable pH-responsive drug delivery and enhanced tumor inhibition, Adv. Funct. Mater. 29 (2019) 1808146, https://doi.org/10.1002/adfm.201808146.
[49] Y. Sun, X. Yang, Z. Wu, Y. Wan, Q. Wei, Q. Hu, Y. Guo, Additive application for modulating physicochemical properties and antitumor effects of $CaCO_3$

nanodelivery systems, J. Drug Deliv. Sci. Technol. 100 (2024) 106080, https://doi.org/10.1016/j.jddst.2024.106080.
[50] Z. Zou, I. Polishchuk, L. Bertinetti, B. Pokroy, Y. Politi, P. Fratzl, W.J.E. M. Habraken, Additives influence the phase behavior of calcium carbonate solution by a cooperative ion-association process, J. Mater. Chem. B 6 (2018) 449–457, https://doi.org/10.1039/C7TB03170J.
[51] Z. Zou, L. Bertinetti, Y. Politi, P. Fratzl, W.J.E.M. Habraken, Control of polymorph selection in amorphous calcium carbonate crystallization by poly(aspartic acid): two different mechanisms, Small 13 (2017) 1603100, https://doi.org/10.1002/smll.201603100.
[52] Q. Wang, W. Huang, J. Wang, F. Long, Z. Fu, J. Xie, Z. Zou, Stabilization and crystallization mechanism of amorphous calcium carbonate, J. Colloid Interface Sci. 680 (2025) 24–35, https://doi.org/10.1016/j.jcis.2024.11.076.
[53] W. Huang, Q. Wang, W. Chi, M. Cai, R. Wang, Z. Fu, J. Xie, Z. Zou, Multiple crystallization pathways of amorphous calcium carbonate in the presence of poly (aspartic acid) with a chain length of 30, CrystEngComm 24 (2022) 4809–4818, https://doi.org/10.1039/D2CE00328G.
[54] Y. Nahmias, G. Yazbek Grobman, N. Vidavsky, Inhibiting pathological calcium phosphate mineralization: implications for disease progression, ACS Appl. Mater. Interfaces 16 (2024) 18344–18359, https://doi.org/10.1021/acsami.3c17717.
[55] P. Wang, S.-W. Yook, S.-H. Jun, Y.-L. Li, M. Kim, H.-E. Kim, Y.-H. Koh, Synthesis of nanoporous calcium phosphate spheres using poly(acrylic acid) as a structuring unit, Mater. Lett. 63 (2009) 1207–1209, https://doi.org/10.1016/j.matlet.2009.02.033.
[56] A. Adamiano, M. Iafisco, M. Sandri, M. Basini, P. Arosio, T. Canu, G. Sitia, A. Esposito, V. Iannotti, G. Ausanio, E. Fragogeorgi, M. Rouchota, G. Loudos, A. Lascialfari, A. Tampieri, On the use of superparamagnetic hydroxyapatite nanoparticles as an agent for magnetic and nuclear *in vivo* imaging, Acta Biomater. 73 (2018) 458–469, https://doi.org/10.1016/j.actbio.2018.04.040.
[57] B. Ghaemi, M. Javad Hajipour, Tumor acidic environment directs nanoparticle impacts on cancer cells, J. Colloid Interface Sci. 634 (2023) 684–692, https://doi.org/10.1016/j.jcis.2022.12.019.
[58] M. Hu, J. Chen, S. Liu, H. Xu, The acid gate in the lysosome, Autophagy 19 (2023) 1368–1370, https://doi.org/10.1080/15548627.2022.2125629.
[59] A. Bigi, G. Falini, E. Foresti, A. Ripamonti, M. Gazzano, N. Roveri, Magnesium influence on hydroxyapatite crystallization, J. Inorg. Biochem. 49 (1993) 69–78, https://doi.org/10.1016/0162-0134(93)80049-F.
[60] Q. Liu, Z. Chen, H. Pan, B.W. Darvell, J.P. Matinlinna, Effect of magnesium on the solubility of hydroxyapatite, Eur. J. Inorg. Chem. 2016 (2016) 5623–5629, https://doi.org/10.1002/ejic.201601056.
[61] X. Yang, B. Xie, L. Wang, Y. Qin, Z.J. Henneman, G.H. Nancollas, Influence of magnesium ions and amino acids on the nucleation and growth of hydroxyapatite, CrystEngComm 13 (2011) 1153–1158, https://doi.org/10.1039/C0CE00470G.
[62] C. De Stefano, A. Gianguzza, D. Piazzese, S. Sammartano, Quantitative parameters for the sequestering capacity of polyacrylates towards alkaline earth metal ions, Talanta 61 (2003) 181–194, https://doi.org/10.1016/S0039-9140(03)00249-2.
[63] B. Kriwet, T. Kissel, Interactions between bioadhesive poly(acrylic acid) and calciumions, Int. J. Pharm. 127 (1996) 135–145, https://doi.org/10.1016/0378-5173(95)04098-6.
[64] N.C. Blumenthal, A.S. Posner, J.M. Holmes, Effect of preparation conditions on the properties and transformation of amorphous calcium phosphate, Mater. Res. Bull. 7 (1972) 1181–1189, https://doi.org/10.1016/0025-5408(72)90097-9.
[65] R. Gelli, P. Tempesti, F. Ridi, P. Baglioni, Formation and properties of amorphous magnesium-calcium phosphate particles in a simulated intestinal fluid, J. Colloid Interface Sci. 546 (2019) 130–138, https://doi.org/10.1016/j.jcis.2019.03.060.
[66] A. Chandrasekar, S. Sagadevan, A. Dakshnamoorthy, Synthesis and characterization of nano-hydroxyapatite (n-HAP) using the wet chemical technique, Int. J. Phys. Sci. 8 (2013) 1639–1645, https://doi.org/10.5897/IJPS2013.3990.
[67] F. Najafizadeh, M.A.S. Sadjadi, S.J. Fateami, M.K. Mobarakeh, R.M. Afshar, The effects of silica and A nature polymer on the size and properties of nano-hydroxyapatite, Orient. J. Chem. 32 (2016) 1639–1647, https://doi.org/10.13005/ojc/320341.
[68] D. Kuila, G.A. Blay, R.E. Borjas, S. Hughes, P. Maddox, K. Rice, W. Stansbury, N. Laurel, Polyacrylic acid (poly-A) as a chelant and dispersant, J. Appl. Polym. Sci. 73 (1999) 1097–1115, https://doi.org/10.1002/(SICI)1097-4628(19990815)73:7<1097::AID-APP2>3.0.CO;2-F.
[69] D.M. Changa, The binding of free calcium ions in aqueous solution using chelating agents, phosphates and poly(acrylic acid), J. Am. Oil Chem. Soc. 60 (1983) 618–622, https://doi.org/10.1007/BF02679800.
[70] S. Mantha, A. Glisman, D. Yu, E.P. Wasserman, S. Backer, Z.-G. Wang, Adsorption isotherm and mechanism of Ca2+ binding to polyelectrolyte, Langmuir 40 (2024) 6212–6219, https://doi.org/10.1021/acs.langmuir.3c03640.
[71] M. Satoh, M. Hayashi, J. Komiyama, Competitive counterion binding and hydration change of Na poly(acrylate)/$MgCl_2$, $CaCl_2$ in aqueous solution, Polymer 31 (1990) 501, https://doi.org/10.1016/0032-3861(90)90393-D.
[72] M. Wallace, J. Holroyd, A. Kuraite, H. Hussain, Does it bind? A method to determine the affinity of calcium and magnesium ions for polymers using 1HNMR spectroscopy, Anal. Chem. 94 (2022) 10976–10983, https://doi.org/10.1021/acs.analchem.2c01166.
[73] S. Cukrowicz, M. Sitarz, K. Kornaus, K. Kaczmarska, A. Bobrowski, A. Gubernat, B. Grabowska, Organobentonites modified with poly(acrylic acid) and its sodium salt for foundry applications, Materials 14 (2021) 1947, https://doi.org/10.3390/ma14081947.
[74] N.M. Sundaram, N. Rajendran, Biodegradation and cytotoxicity of ciprofloxacin-loaded hydroxyapatite-polycaprolactone nanocomposite film for sustainable bone implants, Int. J. Nanomed. 10 (2015) 119–127, https://doi.org/10.2147/IJN.S79995.
[75] J.J. Maurer, D.J. Eustace, C.T. Ratcliffe, Thermal characterization of poly(acrylic acid), Macromolecules 20 (1987) 196–202, https://doi.org/10.1021/ma00167a035.
[76] M.A. Moharram, M.A. Allam, Study of the interaction of poly(acrylic acid) and poly (acrylic acid-poly acrylamide) complex with bone powders and hydroxyapatite by using TGA and DSC, J. Appl. Polym. Sci. 105 (2007) 3220–3227, https://doi.org/10.1002/app.26267.
[77] S. Somrani, C. Rey, M. Jemal, Thermal evolution of amorphous tricalcium phosphate, J. Mater. Chem. 13 (2003) 888–892, https://doi.org/10.1039/b210900j.
[78] J. Vecstaudza, M. Gasik, J. Locs, Amorphous calcium phosphate materials: formation, structure and thermal behaviour, J. Eur. Ceram. Soc. 39 (2019) 1642–1649, https://doi.org/10.1016/j.jeurceramsoc.2018.11.003.
[79] D. Griesiute, L. Sinusaite, A. Kizalaite, A. Antuzevics, K. Mazeika, D. Baltrunas, T. Goto, T. Sekino, A. Kareiva, A. Zarkov, The influence of Fe^{3+} doping on thermally induced crystallization and phase evolution of amorphous calcium phosphate, CrystEngComm 23 (2021) 4627–4637, https://doi.org/10.1039/D1CE00371B.
[80] B. Tian, S. Liu, S. Wu, W. Lu, D. Wang, L. Jin, B. Hu, K. Li, Z. Wang, Z. Quan, pH-responsive poly (acrylic acid)-gated mesoporous silica and its application in oral colon targeted drug delivery for doxorubicin, Colloids Surf. B Biointerfaces 154 (2017) 287–296, https://doi.org/10.1016/j.colsurfb.2017.03.024.
[81] H. Peng, R. Dong, S. Wang, Z. Zhang, M. Luo, C. Bai, Q. Zhao, J. Li, L. Chen, H. Xiong, A pH-responsive nano-carrier with mesoporous silica nanoparticles cores and poly(acrylic acid) shell-layers: fabrication, characterization and properties for controlled release of salidroside, Int. J. Pharm. 446 (2013) 153–159, https://doi.org/10.1016/j.ijpharm.2013.01.071.
[82] H. Wang, W. Bo, X. Feng, J. Zhang, G. Li, Y. Chen, Strategies and recent advances on improving efficient antitumor of lenvatinib based on nanoparticle delivery system, Int. J. Nanomed. 19 (2024) 5581–5603, https://doi.org/10.2147/IJN.S460844.
[83] C. Pacheco, A. Baião, T. Ding, W. Cui, B. Sarmento, Recent advances in long-acting drug delivery systems for anticancer drug, Adv. Drug Deliv. Rev. 194 (2023) 114724, https://doi.org/10.1016/j.addr.2023.114724.